Energy & Environmental Science

ROYAL SOCIETY OF CHEMISTRY

PAPER

View Article Online
View Journal | View Issue

Cite this: *Energy Environ. Sci.*, 2025, **18**, 6764

High-areal-capacity Na-ion battery electrode with high energy and power densities by simultaneous electrospinning-spraying fabrication†

Mengzheng Ouyang, ‡*[a] Zhenyu Guo, ‡[b] Luis E Salinas-Farran,[a] Yan Zhao,[c] Siyu Zhao,[de] Kaitian Zheng,[bf] Hao Zhang,[eg] Mengnan Wang,[b] Guangdong Li,[ah] Feiran Li,[a] Xinhua Liu,[i] Shichun Yang,[i] Fei Xie,[j] Paul R. Shearing,[e] Maria-Magdalena Titirici[b] and Nigel P. Brandon[a]

Received 12th March 2025,
Accepted 23rd May 2025

DOI: 10.1039/d5ee01444a

rsc.li/ees

Sodium-ion batteries (SIBs) are cost-effective alternatives to lithium-ion batteries (LIBs), but their low energy density remains a challenge. Current electrode designs fail to simultaneously achieve high areal loading, high active content, and superior performance. In response, this work introduces an ideal electrode structure, featuring a continuous conductive network with active particles securely trapped in the absence of binder, fabricated using a universal technique that combines electrospinning and electrospraying (co-ESP). We found that the particle size must be larger than the network's pores for optimised performance, an aspect overlooked in previous research. The free-standing co-ESP $Na_2V_3(PO4)_3$ (NVP) cathodes demonstrated state-of-the-art 296 mg cm^{-2} areal loading with 97.5 wt% active content, as well as remarkable rate-performance and cycling stability. Co-ESP full cells showed uncompromised energy and power densities (231.6 W h kg^{-1}/7152.6 W kg^{-1}), leading among reported SIBs with industry-relevant areal loadings. The structural merit is analysed using multi-scale X-ray computed tomography, providing valuable design insights. Finally, the superior performance is validated in the pouch cells, highlighting the electrode's scalability and potential for commercial application.

Broader context

Rechargeable batteries power everything from personal electronics to electric vehicles, playing a crucial role in the shift toward clean energy. In large-scale energy storage systems, however, cost remains a major hurdle—especially when relying on lithium. Sodium-ion batteries (SIBs) provide a promising, more abundant, and cost-effective alternative. Among the available SIB cathode materials, $Na_3V_2(PO_4)_3$ (NVP) is particularly notable for its strong stability and excellent rate capability. However, its low energy density remains a key obstacle to broader adoption. Numerous electrode design approaches—such as increasing areal loading, raising active material content, and removing current collectors—have been investigated to boost energy density. Yet, despite extensive research, no single design has managed to combine high energy and power densities, long-term cycling stability, and industrial scalability. These limitations stem from intrinsic trade-offs among the requirements. Developing a new electrode structure that meets all these criteria is therefore of urgent importance. Our work tackles this issue by proposing a new electrode structure and fabrication process that overcomes these limitations, representing a significant advance not only for SIBs but also for other secondary battery systems.

[a] *Department of Earth Science and Engineering, Imperial College London, London, UK. E-mail: mo113@ic.ac.uk*
[b] *Department of Chemical Engineering, Imperial College London, London, UK*
[c] *Department of School of Energy and Engineering, Jiangsu University, Zhenjiang, China*
[d] *Department of Chemical Engineering, University College London, London, UK*
[e] *Department of Engineering Science, University of Oxford, Oxford, UK*
[f] *School of Chemical Engineering and Technology, Tianjin University, Tianjin, China*
[g] *Department of Chemical Engineering, Massachusetts Institute of Technology, Cambridge, MA, USA*
[h] *School of Chemistry and Chemical Engineering, Beijing Institute of Technology, Beijing, China*
[i] *School of Transportation Science and Engineering, Beihang University, Beijing, China*
[j] *Institute of Physics, Chinese Academy of Science, Beijing, China*

† Electronic supplementary information (ESI) available. See DOI: https://doi.org/10.1039/d5ee01444a

‡ These authors contributed equally to this work.

Introduction

Sodium-ion batteries (SIBs) have emerged as a cost-efficient and sustainable alternative of lithium-ion batteries (LIBs).[1] However, their application is significantly hindered by the lower energy density of existing cathode materials.[2] $Na_2V_3(PO_4)_3$ (NVP) is recognized as one of the most promising cathode candidates due to its high working voltage, high Na^+ conductivity and superior cycling stability.[3] Yet, it suffers from low electron conductivity and a limited theoretical capacity of 117 mA h g^{-1}. Additionally, most reported SIBs have areal loadings far below industrial demands, with high-areal-loading SIB electrodes typically around 10 mg cm^{-2} (ref. 4–6) and a maximum of 60 mg cm^{-2},[7] compared to up to 170 mg cm^{-2} for LIBs.[8,9] This discrepancy is due to the underdeveloped state of cathode materials and structures, further widening the energy density gap between SIBs and LIBs.

There are three effective strategies to enhance an electrode's energy density:[10,11] (i) applying high active materials areal loading, (ii) eliminating the current collector, and (iii) increasing the active materials content (weight ratio of active materials in the whole electrode). All these strategies require carefully designed electrode microstructures. Conventional structures, with randomly-aligned polymeric binders of reasonable weight content, are not strong enough to support such electrodes.[9,12–14] Their highly tortuous electron and ion transportation pathways significantly lower the electrochemical performances.[15]

No reports to date have detailed a high-performance electrode design successfully implementing all three strategies[10,16] (free-standing electrode with >50 mg cm^{-2} areal loading and >95 wt% active content). Those implement one or two of these strategies often sacrifice power densities and stabilities to achieve high energy densities.[9,17]

The challenges stem from the inherent trade-offs in existing electrode structures:

An electrode with high active content struggles to achieve high areal loading/free-standing structure,[9,10,16] or to achieve good performance, due to the insufficient structure support and electron conductivity. *Vice versa*, free-standing and high-areal-loading electrodes usually have active contents below 80 wt%.[18–20]

Achieving high electron and ion conductivity simultaneously is challenging.[21,22] A high content of carbon black/binders will inevitably reduce the porosity and increase pore tortuosity.

It is difficult to further enhance cell performance based on the existing electrode structures. Any novel structures need to meet the following prerequisites: a highly conductive network with both horizontal and vertical robustness, a low-tortuosity pore network that can access all the particle surface, and active particles that are evenly distributed and firmly attached to the conductive network.

While electrospinning is an ideal and scalable method to fabricate such networks,[23,24] an optimal approach for introducing active particles has not been identified. Particles introduced within the electrospun fibres[25] would leave unnecessarily high porosity ($>90\%$) and thus low energy density.[23,26] Introducing the particles into the electrospun network[27] would exclude the use of commercially-available large particles, and would require additional binder/conductive additives, leading to inferior performance.[28,29] Both routes have resulted in electrodes with lower active contents than the conventional electrodes, with no obvious improvement in energy/power density.

In this study, we synthesized an ideal Na-ion battery electrode structure by introducing the active particles through electrospraying simultaneously with electrospinning, a method termed co-electrospinning–electrospraying, or co-ESP. Both methods are highly scalable techniques.[30]

While previous efforts of combining electrospinnig and spraying did not fabricate electrodes with state-of-art performance,[31,32] this work shows that the overlooked particle size effect and the absence of binder/conductive additives are keys to achieving good performance. When the electrosprayed particles are significantly larger than the pores of the electrospun fibre network, they are strongly bound through spatial constrictions without binders, promoting the interphase contact while exposing the particle surfaces to electrolyte. This allows a carbon nanotube-embedded carbon nanofibre (CNTF) network to function as the conductive additive, binder and current-collector with only 2.5 wt% content.

The synthesized high-active-content, free-standing and binder-free electrodes for Na-ion batteries met all the prerequisites and showed one of the best performances at high-areal loading among all reported Li-ion and Na-ion battery electrodes. With 97.5 wt% carbon-coated $Na_2V_3(PO4)_3$ (NVPC) content, the electrodes demonstrated record-high stable areal loading (up to 296 mg cm^{-2} for NVPC, 120 mg cm^{-2} for hard carbon) and rate performance (200C at 4 mg cm^{-2} and 5C at 296 mg cm^{-2}). The electrodes exhibited low polarization, high capacity retention and cycling stability, and state-of-art energy density/power densities across all areal loadings, in both half-cells and full cells. With the assistance of multiscale synchrotron-based X-ray computed tomography, we found that the superior performance was linked with the ideal pore structures, high electron accessibility, and hierarchically porous particles. Finally, pouch cells with capacities up to 200 mA h were assembled using co-ESP electrodes and cycled for 1000 cycles (361 days) with high capacity retention, demonstrating their scaling-up potential.

Results and discussion

The co-ESP fabrication of electrodes

Fig. 1 illustrates the schematics of the co-electrospinning-spraying (co-ESP) set-up. The electrospinning slurries were mixtures of polyacrylonitrile (PAN), and carbon nanotube (CNT) in a dimethylformamide (DMF) solvent, where PAN served as the electrospinning carrier and carbon precursor. The electrospraying slurries were mixtures of polyethylene oxide (PEO) and commercial NVPC particles in DMF, with PEO functioning as both the electrospraying carriers and dispersant.

The areal loadings (thicknesses) of the electrodes were controlled by the total volume of slurries, and the active contents were controlled by the volume ratios of electrospinning/spraying

slurries. The detailed fabrication process is summarized in the Method section and illustrated in Fig. S1 (ESI†), with an accompanying video provided in Video S1 (ESI†).

In contrast to conventional electrosprayed battery electrodes, which use metal salt solutions,[33] we employed a highly concentrated suspension. This accelerated the electrospraying of NVPC by over tenfold,[34] aligning its rate with the electrospinning to achieve the desired active content. This change also ensured a comparable fabrication time with the conventional slurry-casting and drying process.

Following co-ESP, the mats were calcined to remove the PEO and pyrolyze the PAN. The resulting electrodes, shown in Fig. 1b, exhibited remarkable flexibility and a fabric-like texture. Notably, our lab-scale process is capable of fabricating electrodes with up to 600 cm^2 per batch (Fig. 1b), enough for 300 CR2032 coin cells, highlighting co-ESP's strong potential for scaling up.

Regarding morphology, Fig. 1c shows that the co-ESP electrode consisted of a percolating, inter-supported network of CNT-embedded CNF (CNTF), which homogeneously encapsulated the NVPC cathode particles. The morphologies of NVPC particles and co-ESP NVPC electrodes, both as-fabricated and post-pyrolysis, are detailed in Fig. S2 (ESI†). The fibres, with diameters of approximately 150 nm and lengths of up to 1 cm (Fig. S3, ESI†),[35] are two orders of magnitudes longer than the CNTs typically used in battery electrodes.[9,36] Such a high length-to-diameter ratio is beneficial to the formation of robust supporting backbones at low mass contents,[37,38] while leaving sufficient porosity. CNT was embedded into the PAN-derived CNF, with a weight content of 40 wt%[39,40] (Fig. S4 and S5, ESI†), which is significant given the low percolation threshold of aligned CNTs.[41] In Fig. S5 (ESI†) we have shown *via* TEM that the inside of PAN-derived CNF is filled with CNT, which confirmed that CNTs fully percolate inside the PAN-derived CNF, aligned along the fibre direction. Previous research found that the CNTs exhibit 10^5 times higher conductivity than the polymer-derived CNFs, and they also enhance the graphitization of these CNFs.[40] As a result, it enhanced the network's conductivity by an order of magnitude (Fig. S6, ESI†). The Raman spectrum of co-ESP NVPC and hard carbon electrodes indicated a higher degree of graphitization than typical PAN-derived carbon pyrolyzed at the same temperature (Fig. S7, ESI†).

The size effect of co-ESP electrodes

Notably, the co-ESP method allowed for the introduction of particles larger than the pores of the fibre network (Fig. 1e). This enabled strong particle binding through the spatial constraints of the network, thus eliminating the need for binders and conductive additives. The average NVPC particles size was 20 μm, significantly larger than the average pore size of the CNTF network (2 μm) (Fig. S8 and S9, ESI†). Consequently, this network fulfils the roles of conductive additive, binder, and current collector, while also providing adequate porosity for electrolyte immersion. In contrast, when particles smaller than the pore sizes were introduced, as shown in Fig. 1d, they were poorly bound to the network, while resulting in insufficient electrical contact (Fig. 1f).

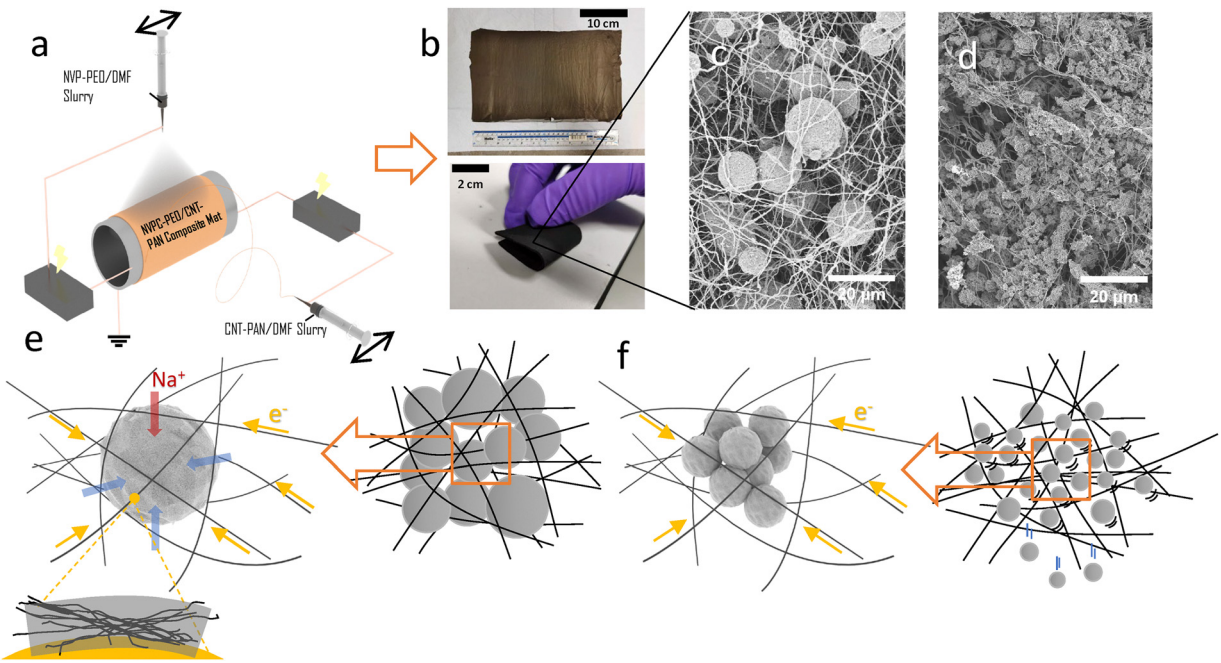

Fig. 1 Fabrication and 2D morphology of the co-esp NVPC/CNTF electrodes. (a) Schematic diagram of co-electrospinning–electrospraying fabrication set-up. (b) Photographic pictures of 600 cm^2 as-spun NVPC-PEO/CNT-PAN electrode (above) and calcined 20 cm^2 co-esp NVPC/CNF electrode (below, containing weight ratio of CNT : CNF : NVPC of 1 : 1.5 : 97.5). SEM images of co-esp electrodes with (c). Pristine micron-sized NVPC particles and (d). Ball-milled nano-sized NVPC particles. The schematic diagrams of the NVPC/CNTF co-ESP electrode (e). Composed of pristine micron-sized NVPC particles; (f). Composed of ball-milled NVPC particles.

To confirm the importance of particle sizes, small NVPC particles were produced by mildly ball-milling the pristine NVPC particles (Fig. 1d). The average diameter of ball-milled particles (300 nm) was well below the average pore size of electrospun fibre network (2 μm) (Fig. S9, ESI†). The ball-milling did not induce any crystal structure changes or impurities (Fig. S10, ESI†), which can occur under harsher milling condition.[42] 1. Any impurity phases that might have been introduced during milling would likely have been converted to the thermodynamically stable NVPC phase during the heat-treatment. The crystalline sizes remained unchanged, confirming that the ball-milling only broke down the secondary particles.[43] Na-ion half-cells were assembled with pristine and ball-milled co-ESP NVPC cathodes of 18 mg cm^{-2}, 97.5 wt% active loading (1.5 wt% CNF/1 wt% CNT) (Fig. 2a).

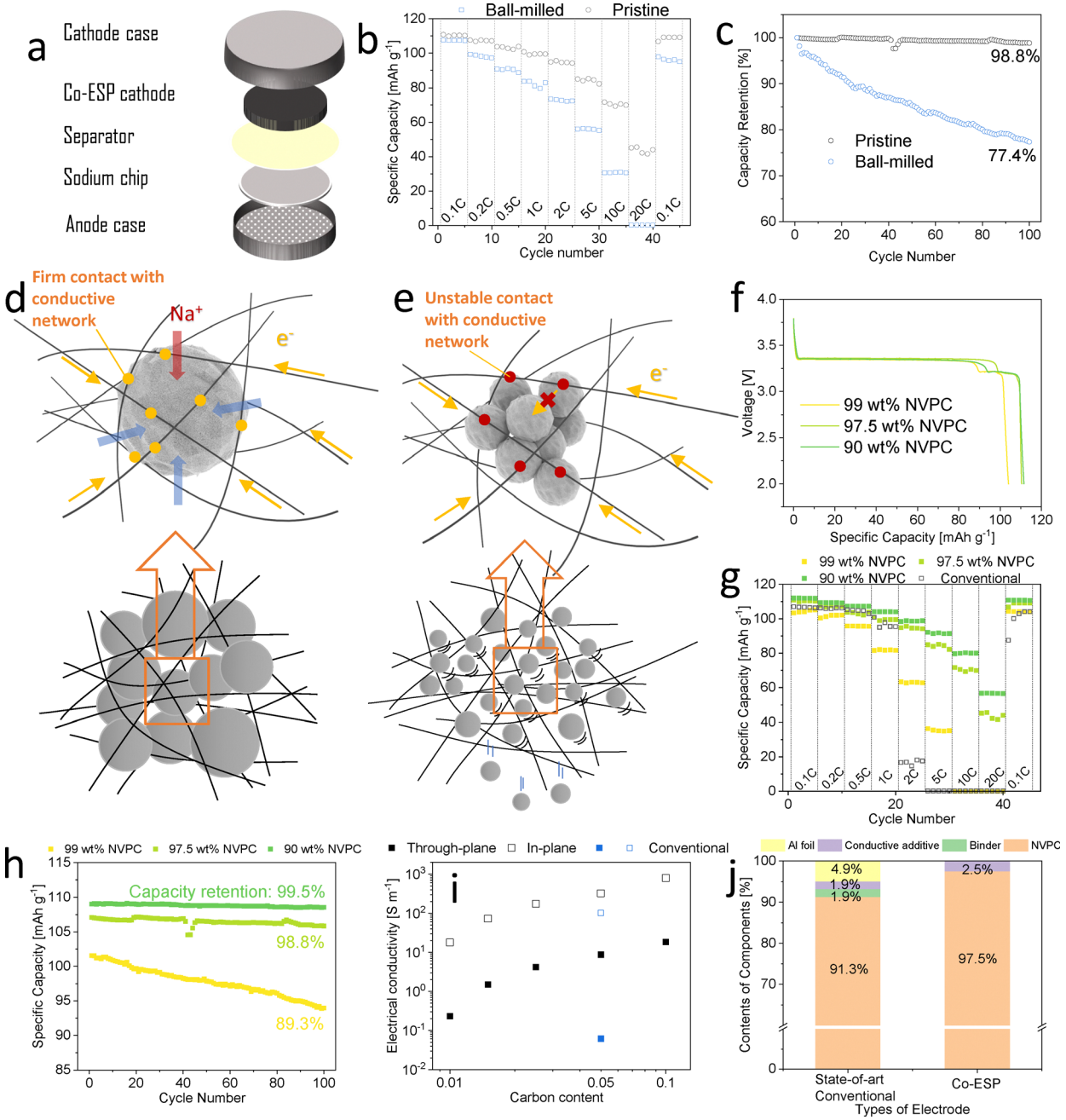

Fig. 2 The performance of co-ESP NVPC cathodes with different particle sizes and active content: (a) schematic diagram of a sodium-ion battery half cell; half cell performance of co-ESP NVPC cathode consist of pristine and ball-milled NVPC: (b) rate performance and (c) 0.2C cycling stability; the schematic diagrams of the morphology and electron transportation path of NVPC/CNTF co-ESP electrode with (d) pristine NVPC particles and (e) ball-milled NVPC particles; half cell performance of co-ESP NVPC with different active contents: (f) the third discharge curve and (g) rate performance and (h) 0.2C cycling stability; (i) electric conductivity of co-ESP NVPC electrode with different CNTF content component's; (j) composition of co-ESP and state-of-the-art conventional slurry-casted NVPC cathode with 25 mg cm^{-2} areal loading.

Both electrodes showed near theoretical initial discharge capacities under 0.1C. The ball-milled electrode showed a higher capacity (117 *vs.* 110 mA h g^{-1}) but a lower initial coulombic efficiency (ICE) of (93.8% *vs.* 97.7%) of the pristine electrode (Fig. S11, ESI†). The higher capacity further proved that that ball-milling did not introduce phase impurity that could affect the performance of the electrode. The lower ICE was likely due to more sodium being consumed in the formation of the cathode-electrolyte interface (CEI) on the ball-milled particles.[44] Additionally, ball-milled electrode demonstrated poorer rate performance (Fig. 2b). The pristine co-ESP NVPC electrode retained 72.1% and 36.8% of its theoretical capacity at 5C and 20C, respectively, while the ball-milled electrode retained 47.8% and 0%, respectively. The conductivities of the electrodes before and after ball-milling were similar (Fig. S12, ESI†), indicating the particle sizes did not affect the percolation of CNTF network. The conventional electrode with ball-milled NVPC showed similar voltage profile with pristine particles (Fig. S13, ESI†), suggesting the electrochemical properties did not deteriorate with ball-milling.

After 100 cycles at 0.2C, the ball-milled electrode showed 77.4% capacity retention, notably lower than the 99.6% retention of the pristine electrode (Fig. 2c). Post-cycling, the ball-milled electrode was partly disintegrated, with small NVPC particles detaching the CNTF network, whereas the pristine electrode's morphology remained intact (Fig. S14, ESI†). The robustness of the co-ESP electrodes were also demonstrated through sonication (Video S2 and S3, ESI†). Powders detached from the ball-milled electrode from the start, while the pristine electrode remained intact throughout the sonication process. Nevertheless, both electrodes exhibited significantly better rate performance than the conventional slurry-casted electrode (Fig. 2g).

The poorer rate performance and cycling stability of the ball-milled electrodes are attributed to the weaker binding of smaller particles. Unlike the pristine particles (Fig. 2d), the ball-milled particles were much smaller than the pore of the CNTF network and were not bound by spatial constrictions (Fig. S8 and S9, ESI†). These particles were only loosely attached to the CNTF network, resulting in high contact resistance. Additionally, not all particles were directly in contact with the conductive network, requiring electrons to traverse multiple particle–particle interfaces to reach these particles, further increasing resistance[45,46] (Fig. 2e). Since the ion diffusion and insertion/extraction should be quicker as particles became smaller,[45] the poor rate performance of the ball-milled electrode was likely because of the poor electronic conduction. Therefore, CNTF network is especially ideal for capsulating commercial electrode materials of Li and Na-ion batteries, most of which have secondary particle sizes of 5–50 μm.[47] To demonstrate this, we have fabricated co-ESP LiFePO4-C LIB cathode, SiOx-C and graphite LIB anodes, as shown in Fig. S15 (ESI†). The voltage profiles of these electrodes are shown in Fig. S16 (ESI†). All electrodes showed high areal capacities, high specific capacities, and small overpotential.

Previous attempts to fabricate battery electrodes using combinations of electrospin and spray have not demonstrated competitive areal loading, active content, rate performance, or cycling stability compared to other state-of-the-art techniques.[31,32] This is likely because nano-sized particles were used. Additional binder/conductive additives were added to stabilize the particles, which further deteriorated the performance and significantly reduced the active content. There was also no in-depth analysis of the merit of the co-ESP method and the resulting structures in previous works, which we are aiming to do here. Given the significantly superior performance, we will only use pristine micron-sized NVPC in the co-ESP NVPC electrodes for the remainder of this work.

Performance of co-ESP electrodes with different CNTF content

Given the critical role of the CNTF network, it is important to investigate its minimum content required to provide sufficient electron conductivity and structural support, thereby achieving the highest energy density. We synthesized electrodes with active contents of 90 wt%, 97.5 wt%, and 99 wt% (Table S1, ESI†), all with areal loadings of *ca.* 18 mg cm^{-2}. Electrodes with active content above 99% were too fragile for use in cells. As shown in Fig. S17 (ESI†), increasing the active content resulted in sparser fibres. In the 99 wt% electrode not all particles were in direct contact with the CNTF network.

At 0.1C, 97.5 wt% and 90 wt% electrodes showed similar discharge capacity and polarization, while the 99 wt% electrode had lower discharge capacity and discharge plateau (Fig. 2f). The capacity difference became more pronounced with an increasing C-rate. At 10C, the 99 wt% electrode showed no discharge capacity (Fig. 2g). In contrast, both the 97.5 wt% and 90 wt% electrodes maintained decent capacities even at 20C. All electrodes demonstrated superior rate performance compared to conventional electrodes.

Apart from lower rate performance, 99 wt% electrode also showed lower cycling stability than its lower active content counterparts (Fig. 2h). Note that the capacity fluctuation of the 97.5 wt%-pristine particle coin cell from the 42nd to 45th cycle in Fig. 2c and h were due to the movement of testing cell by a lab personnel during the cycling, which did not affect the subsequent cycling. These results suggest that 1 wt% CNTF neither provided sufficient electron accessibility for high-rate cycling nor supported the electrode structure adequately. The through plane conductivity of 99 wt% electrode (1.5 S m^{-1}) was lower than 90 wt% (18.5 S m^{-1}) and 97.5 wt% (4.2 S m^{-1}), but was still sufficient according to previous work.[21] However, macroscopic conductivity does not reflect the electron accessibility of individual particles. As shown in Fig. S17 (ESI†), NVPC particles not in direct contact with the CNTF network could not contribute their capacities at high rates. In contrast, active particles in 97.5 wt% and 90 wt% electrodes were all connected to the CNTF network, (Fig. 2i) and had sufficient electron accessibility, shifting the rate-limiting process to ion transportation.[21] This explains why further reducing the active content beyond 97.5 wt% showed only marginal improvement. Thus, 97.5 wt% is the optimal active content for the co-ESP NVPC electrode, balancing performance, electrode robustness, and

active content. We will use this composition throughout the rest of this work. This active content brings 6.7% higher energy/power density than a state-of-the-art commercial 25 mg cm^{-2} electrode (96 wt% NVPC, 2 wt% PVDF, 2 wt% carbon black, 5 μm aluminum foil, Fig. 2j) even without considering the performance benefit of co-ESP electrodes.

Previous efforts to achieve high areal loading and superior rate performance often gave up controls over the active content,[10,18] resulting in overall loss in the energy/power density. The co-ESP electrode, however, has demonstrated an uncompromised solution, maintaining high active content alongside excellent performance, while having an active content significantly higher than other high-loading electrodes.[9,48]

Morphology benefit of co-ESP NVPC electrodes

Co-ESP NVPC electrodes have demonstrated remarkable rate performance and stability with high active contents. To further understand the morphology benefits, synchrotron-based micro- and nano-computed tomography (micro- and nano-CT) were employed to characterize multiscale features of the electrodes (Fig. 3a–f). Micro-CT was used to resolve the morphology of particles and external pores (Fig. 3a and b), with the electrodes characterized in a compressed state to mimic their condition in cells. The nano-CT was used to resolve the particles internal pores (Fig. 3c), though it could not resolve all the CNTFs due to their small diameter relative to the resolution (150 nm *vs.* 47 nm) and the low visibility of carbon materials in the presence of NVPC.[49]

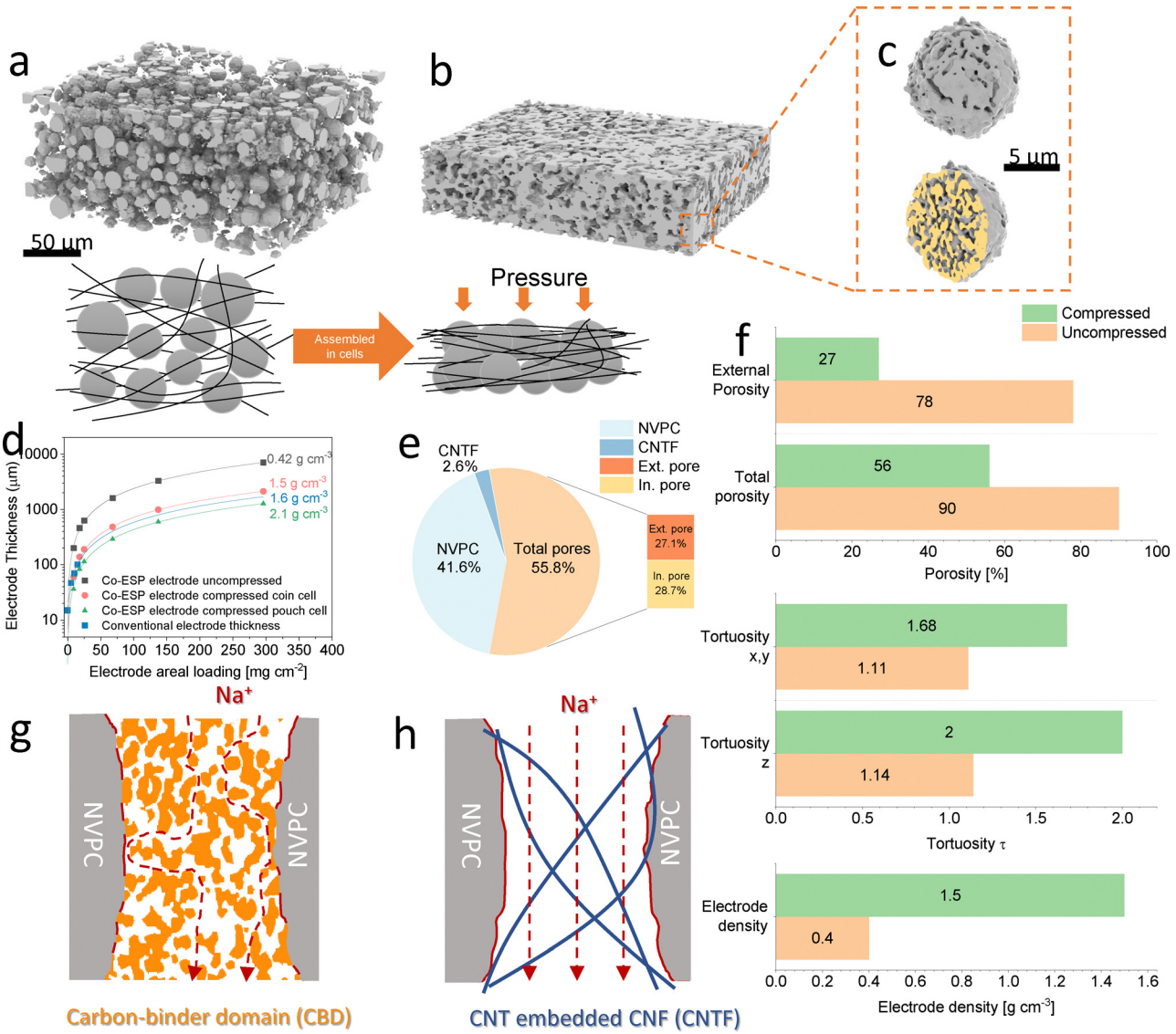

Fig. 3 Physical properties and 3D morphology of co-ESP NVPC electrodes: the schematics and 3D reconstruction of NVPC/CNTF electrodes, reconstructed from micro-CT scans: (a) uncompressed; (b) compressed; (c) fine structure of a single NVPC particle (cross-section indicated in yellow); (d) the thickness of compressed and uncompressed NVPC/CNTF electrodes with different areal loadings and conventional electrodes (current collector included); (e) the volume ratio of different components in a compressed NVPC/CNTF electrode; (f) summary of structural parameters acquired from XCT; the schematics of sodium ion transportation in the pores of (g) conventional electrodes and (h) co-ESP electrodes.

From Fig. 3a, it is evident that the co-ESP NVPC electrode comprises well-distributed large NVPC particles and interconnected pores. A single NVPC particle resolved by the nano-CT (Fig. 3c) revealed an internal porosity of 39.4% with an average pore size of 582 nm, based on an average of 20 particles. All internal pores were percolated and accessible from the particle surface.

Upon compression at 4 MPa, the thickness of the electrodes reduced significantly, as did the volume of external pores (Fig. 3b). The thickness of the co-ESP electrodes was extracted from their compression curve (Fig. S18a, ESI†). Uncompressed, these electrodes were more than four times thicker than conventional slurry-casted cathodes (NVPC : PVDF : CB = 90 : 5 : 5) of the same loading (Fig. 3d), resulting in only 25% of the electrode active density (weight of active materials per volume). After assembly in coin cells, their thickness reduced by 70%, reaching 91% active density of conventional electrodes. Pouch cells electrodes were compressed at 30 Mpa before pyrolysis, resulting in 30% higher electrode density than the conventional electrodes. This is equivalent to 3.1 g cm^{-3} of an NMC111 electrode and 2.4 g cm^{-3} of an LFP electrode, considering the lower density of NVP (3.21 g cm^{-3} (ref. 50)) *versus* NMC111 (4.77 g cm^{-3} (ref. 51)) and LFP (3.6 g cm^{-3} (ref. 52)). Such an electrode density is on par with the state-of-the-art LIB electrodes.

This high compressibility is an essential feature of the co-ESP NVPC electrode. As shown in the cross-section images (Fig. S3, ESI†), the CNTFs tend to align in-plane due to the layered deposition of electrospun fibres. The intrinsic flexibility of CNTFs granted the co-ESP electrode the ability to maintain structural integrity even after 70% strain (Fig. 3b and d), enhancing the contact between the electrode and cases/metal tabs without a current collector. For half cells with the areal loadings higher than 150 mg cm^{-2}, sufficient electric connection between the electrode and the coin cell case can be achieved without the springs and spacers. Fig. S18b (ESI†) shows the compression modulus of a co-ESP NVPC electrode changing with strain. The compression behavior of the co-ESP electrode is not linear, therefore there is no platform area in the modulus curve. When the strain exceeds 55% there is a rapid increase of compression modulus, suggesting the particles/CNTF network are compactified and in good contact with each other. This is in accordance with the low external porosity under 4 MPa pressure. The volume compositions of different electrode components after compression are summarized in Fig. 3e. Note that the external porosity only considered the pores outside the NVPC particles, while total porosity included pores both outside and inside the NVPC particles, acquired from micro-CT and nano-CT respectively. After compression, the electrode had 55.8% total porosity, with external porosity at 27.1%. The porosity was uniform across the cell thickness (Fig. S19, ESI†). The total porosity is higher than most reported electrodes, although previous works rarely considered pores inside particles.[26,53] Therefore, external porosity is a better parameter for comparison. Active particles comprised 94.1 vol% of the solid phase, indicating efficient utilization of the electrode volume.

Other microstructural parameters after compression are summarized in Fig. 3f, with detailed summaries available in Table S2 (ESI†). When uncompressed, the external pore tortuosity of the co-ESP NVPC electrode was *ca.* 1.1, identical across the *x*, *y*, and *z* directions, indicating a homogeneous pore structure. After compression along the *z* direction, the *z*-tortuosity increased to 2.0. Conventional electrodes typically have pore tortuosity of 5–8 due to the presence of carbon binder domain (CBD), which refers to the composite cluster of binder and conductive additive.[53,54] Although CNTFs could not be resolved, they are not expected to significantly increase tortuosity because of their low volume content (<3 vol%) and small diameters relative to external pores (150 nm *vs.* 10 μm, Fig. S3, ESI†). The low *z*-tortuosity ensures smooth through-plane transportation of Na-ions.

In the conventional electrodes the presence of highly tortuous CBD has been proven to be the main reason for sluggish ion transportation in the pore[28,29,55] (Fig. 3g). Even without binder, the nano-sized conductive additives would also significantly increase the pore tortuosity.[56,57] CBD is also the reason that the ion transportation and electron conduction cannot be simultaneously increased in conventional electrodes.[54,58]

The absence of CBD or any nanosized conductive additives in our co-ESP NVPC electrodes significantly accelerated ion transportation, which is the rate-limiting process when electron conduction is sufficient.[21] Additionally, the surface of NVPC particles were fully accessible to sodium ions, maximizing the Na-ion intercalation/insertion interface (Fig. 3h).[59]

The ion transportation was further enhanced by hierarchical internal pores in the NVPC particles (Fig. 3c), which shortened the diffusion pathway of Na-ions in the NVPC solid by approximately 20-fold. This leveraged the fact that sodium diffusion in the electrolyte is at least five orders of magnitude faster than in the solid NVPC phase.[60,61]

For electron conduction, the percolating CNTF network ensures electronic access to all NVPC particles, while the coated carbon on the NVPC guarantees uniform electron accessibility across the particles. Conventional electrodes require at least 5 wt% CBD to ensure carbon black percolation.[62] In contrast, due to the intrinsic interconnecting nature of the CNTF network, there is no theoretical percolation threshold. Good macroscopic electronic conductivity was achieved with even less than 1 wt% CNTF loading, despite the insufficient electron accessibility of individual particles.

The CNTF network also binds the particles through spatial constriction, providing a much stronger binding force than the van der Waals bond of conventional binders.[9] On the other hand, larger particles applied stress to the fibres caging them, securing their electrical contact. Thus, in the co-ESP electrode, high conductivity, fast ion transportation, and robust structure are achieved simultaneously (Fig. 3d, e and Fig. 2i and j) with only 2.5 wt% inactive content. Especially, both electron conduction and ion conduction pathways are minimized, creating an ideal electrode structure as predicted by previous work.[45] Since ion diffusion and electron conductivity have been found to co-limit the performance,[21] this results in the outstanding rate performance and stability of the co-ESP NVPC electrodes.

High areal loading, high-performance half-cells enabled by CNTF network

The co-ESP NVPC electrodes exhibited an intrinsic ability to support high-areal-loading active materials thanks to the inter-supportive nature of the CNTF network. Unlike conventional electrodes, there is no fundamental limitation to the thickness and the areal loadings of co-ESP electrodes. The thickness and areal loading were controlled by adjusting the total amount of raw materials in the co-ESP fabrication process, as detailed in Table S3 (ESI†).

Half-cells were assembled with co-ESP NVPC cathodes of up to 49.6 mg cm^{-2} areal loading (Fig. 2a). Cross-sectional images of co-ESP NVPC electrodes with different areal loadings are shown in Fig. S20 (ESI†). When the areal loading exceeded 50 mg cm^{-2}, the half-cells began to exhibit serious over-charging after 15–20 cycles (Fig. S21, ESI†), preventing further increases in areal loading in half-cells. This was previously attributed to the degradation of metallic anode,[9,63] which is confirmed by the intact structure of the co-ESP NVPC cathodes (Fig. S14, ESI†), and the severe degradation of Na metal anodes (Fig. S22, ESI†) after cycling. The addition of fluoroethylene carbonate (FEC) to the electrolyte slowed degradation but could not eliminate it (Fig. S23, ESI†).[64,65] Thus, the co-ESP electrodes' ability to hold higher areal loading will be demonstrated in full cells.

All co-ESP NVPC electrodes showed state-of-the-art rate performance and cycling stability for their respective areal loadings. At the lowest area loading of 4.3 mg cm^{-2}, co-ESP NVPC electrodes showed decent capacity even at 200C, while the 49.6 mg cm^{-2} electrodes were usable at 10C (Fig. 4a–d). The 4.3 mg cm^{-2} cell was cycled at 50C for 5000 cycles with 84.8% capacity retention, and the 49.6 mg cm^{-2} cell was cycled at 0.2C for 200 cycles with 97.5% capacity retention (Fig. 4e). Note that from Fig. 4a, Coulombic efficiency would drop in the first cycle after increasing the C-rate. This was also commonly observed in previous works.[66,67] At higher currents, the overpotential of the

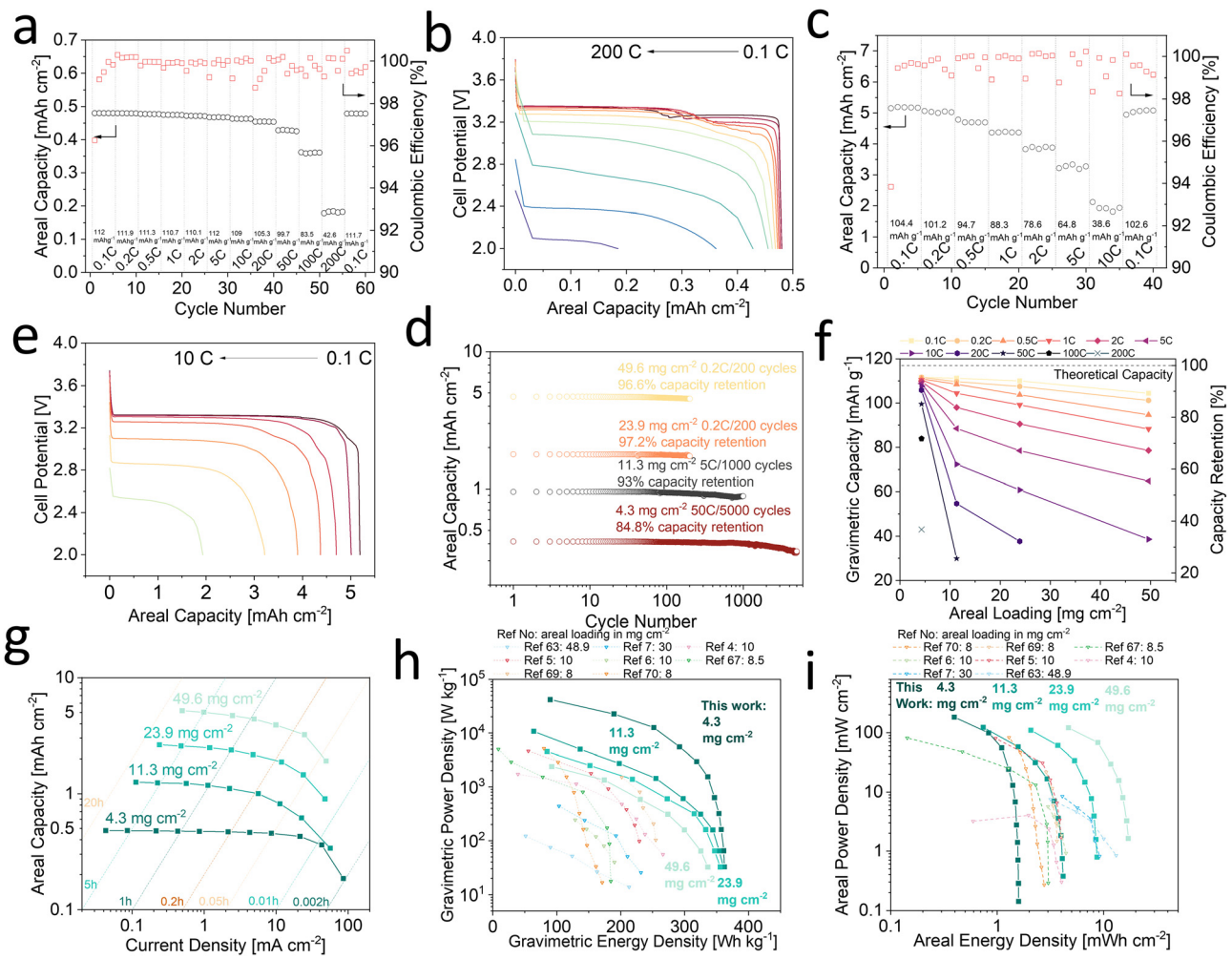

Fig. 4 The performance of co-ESP NVPC cathodes with different areal loading: 4.3 mg cm^{-2} cathode's (a) rate performance and (b) voltage profile; 49.6 mg cm^{-2} cathode's (c) rate performance and (d) voltage profile; (e) cycling stability of different areal loading half cells; (f) the change of specific discharge capacity with areal loading and cycling rate; (g) the change of areal capacity with areal current; Ragone plots of (h) gravimetric energy density *versus* power density and (i) areal energy density *versus* areal power density, including the data acquired from previous sodium-ion battery half cells for comparison.

electrodes increases, leading to higher polarization, which leads to incomplete sodiation/desodiation, resulting in lower Coulombic efficiency. For example, in a NVPC half-cell, in the first cycle of a faster C-rate, the desodiation (charge) is more complete than the sodiation (discharge) due to the CC–CV charging protocol, resulting in a lower Coulombic efficiency. In the second cycle, the desodiation proceeds from the previous less complete sodiation. Therefore, its capacity matches the sodiation capacity, and restores the Coulombic efficiency afterwards.

High areal loading co-ESP NVPC electrodes did not exhibit significantly higher degradation rate than their low loading counterparts, a common issue in other high-areal-loading cathodes.[9,68] This can be attributed to the following factors:

The CNTF network physically bound the NVPC particles and absorbed their volume changes during charge/discharge cycles, avoiding the loss of electron accessibility; The absence of CBD prevented pore clogging by the formation of CEI, preserving fast ion transportation; The combination of the above factors prevented the NVPC particles disintegration caused by the inhomogeneous sodiation.

Thus, the co-ESP electrodes overcame the three main causes of the accelerated degradation in high-areal-loading electrodes.[28] The detailed electrochemical test result across all areal loadings (Fig. S24, ESI†) were summarized into Fig. 4f and g, demonstrate how specific capacities and areal capacities changed with C-rate and areal loading. When cycled at 0.1C, the specific capacities remained almost invariant until the areal loading reached 23.9 mg cm^{-2}. Increasing the loading further to 49.6 mg cm^{-2} reduced the capacity to 89.2% of the theoretical capacity. In comparison, other Na-ion cathode works did not report more than 80% capacity retention for areal loadings above 10 mg cm^{-2}.[7,69] The average discharge voltage is summarized in Fig. S25 (ESI†).

On the other hand, the 4.3 mg cm^{-2} co-ESP NVPC's retained 71.8% of the theoretical capacity at 100C, and 36.4% at 200C. Increasing the areal loading caused the specific capacities to reduce more pronouncedly with increasing C-rate, as expected for all high-areal-loading electrodes.[9,18] However, the 11.3 mg cm^{-2} electrode still retained 25.6% of the theoretical capacity at 50C, while the 49.6 mg cm^{-2} electrode retained 33% at 10C, demonstrating one of the best rate performances at this level of areal loading among all Na and Li-ion batteries[16,70–72] (detailed comparisons in Tables S4 and S5, ESI†).

Fig. 4g shows that 49.6 mg cm^{-2} electrode retained 3.9 and 1.9 mA h cm^{-2} areal capacity at 2C and 10C, respectively, demonstrating that high areal capacity and high charge/discharge current were achieved simultaneously. These state-of-art rate performances and stabilities confirmed the structural merit of co-ESP electrodes.

Electrochemical impedance spectroscopy (EIS) of the electrodes showed low Ohmic resistances across all samples (Fig. S26, ESI†). While ohmic resistance increased with areal loading, the polarization resistance decreased, consistent with previous report.[73] This reduction is mainly due to the reduced charge-transfer resistance for Na intercalation/extraction, facilitated by the higher number of active sites.

The data in Fig. S24 (ESI†) were summarized in two Ragone plots (Fig. 4h and i). Previously reported Na-ion battery half-cell data from the literatures were included in the same figures.[4–7,69,74–77] Note that most literature did not disclose sufficient information to calculate the energy/power densities of the whole cells, such as electrode porosities and the weight of electrolytes and separators. For a better comparison, the half-cell energy/power densities in this work considered only the weight of cathodes, including the current collector. Literatures values were recalculated under the same standard, as presented in Supplementary Appendix 3 (ESI†). The combination of energy/power densities of co-ESP electrodes leads by a noticeable margin among reported Na-ion battery electrodes, attributing to a combination of high capacity retention, high active content, and superior rate performance.

Previously, the highest reported areal loading of Na-ion batteries' cathodes was 60 mg cm^{-2}, where no cycling or rate data were presented.[7] The second highest was 48.9 mg cm^{-2}, which showed much inferior rate performance and cycling stability than the 49.6 mg cm^{-2} co-ESP NVPC electrode.[69]

The half-cells data were also compared with high-areal-loading lithium-ion half-cells (Table S5, ESI†). Although the NVPC co-ESP electrodes' energy densities do not match those of lithium cobalt oxides (LCO) and lithium nickel manganese cobalt oxides (NMC) cathodes, they are comparable to lithium iron phosphate (LFP) cathodes, the second most widely used cathode material in electric vehicles.

Ultra-high loading full cells and pouch cells

Na-ion full cells (coin cells) were assembled using co-ESP NVPC cathodes and co-ESP hard carbon (HC) anodes (Fig. 5a). The high-performance glucose-derived hard carbon (HC) was synthesized through a facile method as detailed in the previous literature.[78] The voltage–capacity profile, cycling stability and rate performance of the co-ESP HC half-cell is demonstrated in Fig. S27 (ESI†). The electrode exhibited great cycling stability, and significantly improved rate performance compared to the same HC in conventional electrodes with much lower areal loading in our previous paper.[78] Similar to the co-ESP NVPC half cells, the areal loading was limited to 16.5 mg cm^{-2} due to problems associated with the sodium metal counter electrode (Fig. S23, ESI†). The composition of fabrication raw materials is presented in Table S6 (ESI†). The PAN-derived CNF, embedded CNT and HC were all active sodium storage materials,[79–81] in which the HC contributed $>97\%$ of the total capacity.

The morphology of the co-ESP HC anode is shown in Fig. S28 (ESI†), where nano-sized HC particles are agglomerated into secondary particles of average size of 9.9 μm, bound by the CNTF networks through spatial constriction, similar to NVPC particles.

By maintaining the cathode/anode mass ratios at 2.5 : 1, we assembled full cells with cathode areal loading ranging from 25.4 mg cm^{-2}, an industry-relevant areal loading, to a record high of 296 mg cm^{-2}. The maximum areal loading of full cells significantly exceeded the half-cells due to the absence of the problematic Na metallic anode. A 296 mg cm^{-2} loading was

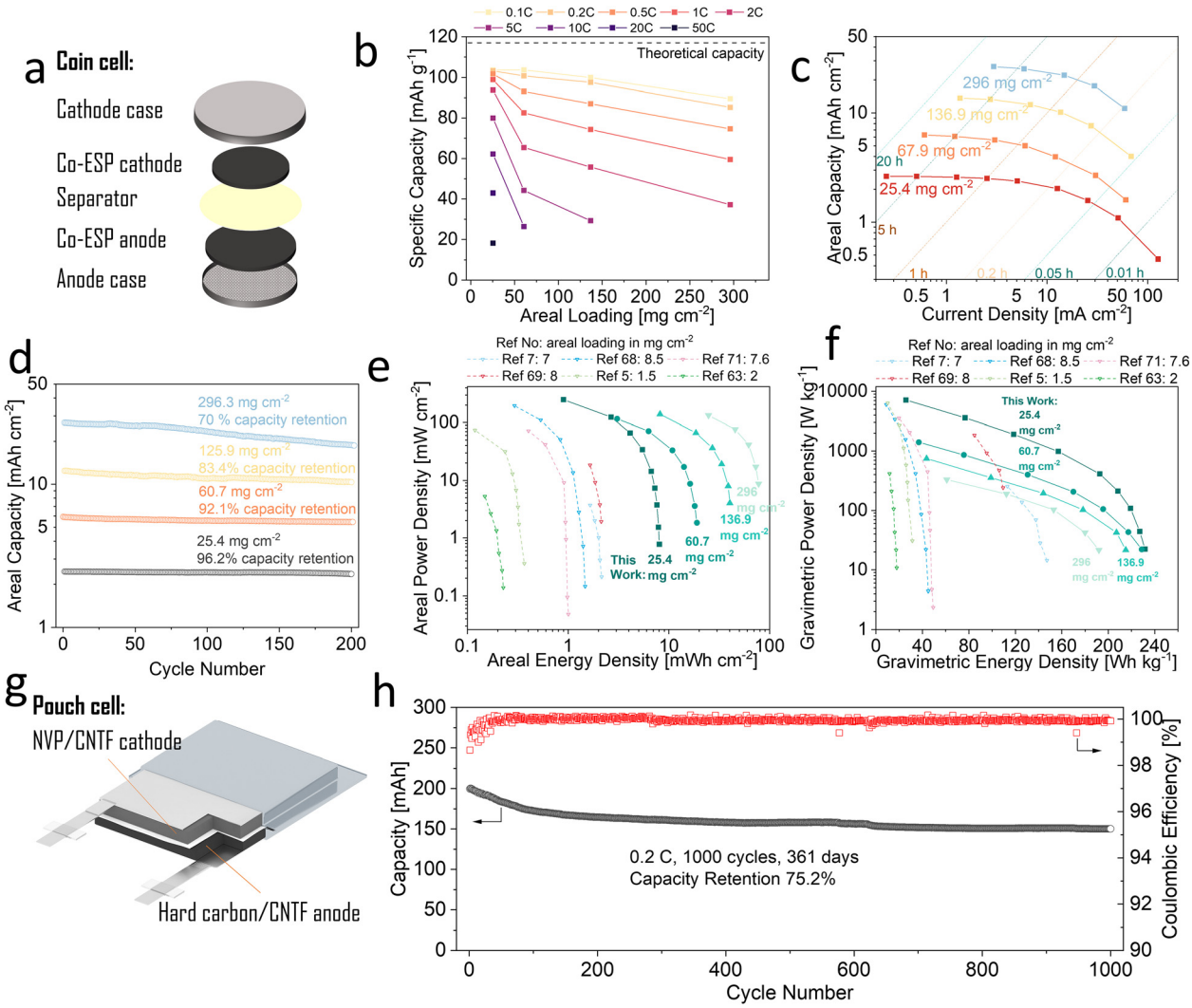

Fig. 5 The performance of sodium ion batteries full cells and pouch cells made of co-ESP NVPC cathodes and co-ESP HC anodes: (a) schematic diagram of a sodium-ion battery full cell; (b) the change of specific discharge capacity with areal loading and cycling rate; (c) the change of areal capacity with areal current; (d) cycling stability of different areal loading full cells; Ragone plots of (e) gravimetric energy density *versus* power density and (f) areal energy density *versus* areal power density, including the data acquired from previous sodium-ion battery full cells for comparison; pouch cell performance with 100 mg cm^{-2} cathode loading: (g) schematic diagram of a sodium-ion battery pouch cell; (h) cycling performance of 0.2 A h, 100 mg cm^{-2} cathode loading pouch cell.

realized by layering two 148 mg cm^{-2} co-ESP NVPC cathodes. In comparison, the conventional electrodes would crack and delaminate from the current collector at areal loadings over 50 mg cm^{-2} (Fig. S29, ESI†). Detailed full cell compositions are shown in Tables S7 and S8 (ESI†), with a typical conventional cell composition provided in Table S9 (ESI†). This represents the highest areal loading to date that can cycle stably among reported Na-ion batteries (Table S10, ESI†) and Li-ion batteries full cells (Table S11, ESI†).

The ICE of the 25.4 mg cm^{-2} full cell was 88.9% (Fig. S30, ESI†). Due to the high ICE of the co-ESP NVPC half-cell, the lower ICE was mainly attributed to the irreversible sodium intercalation to the HC anode and the formation of solid–electrolyte interphase (SEI),[82] which can be enhanced through electrolyte optimisations.[83] The ICE decreased with increasing areal loading, reaching 77% at 296 mg cm^{-2}, likely due to the increased irreversible sodium plating, a common issue for thick anodes.[84] Despite the slower degradation of 296 mg cm^{-2} co-ESP electrode than other high-loading electrode in the literatures, it is significantly faster than its lower loading counterparts, suggesting there is still room to improve. Further work should be focused around optimising the microstructure, screening the electrolyte combination, and systematically correlating capacity retention with areal loading to identify the stability sweet spot.

The co-ESP full cells exhibited superior rate performance (Fig. 5b and c). Detailed electrochemical testing results are available in Fig. S31 (ESI†). The average discharge voltage is shown in Fig. S32 (ESI†). The 25.4 mg cm^{-2} full cells delivered 58% of theoretical capacity at 10C, and 17% capacity at 50C. The full cell with 298 mg cm^{-2} cathode loading exhibited 76.5%

of theoretical capacity at 0.1C. Even at 2C it still delivered 10 mA h cm^{-2}, much higher than a typical conventional electrode (<3 mA h cm^{-2}).

The full cells also exhibited great stability. The 298 mg cm^{-2} loading cell exhibited 73.4% capacity retention after 200 cycles at 0.2C (Fig. 5d and Fig. S31, ESI†). A 60.7 mg cm^{-2} full cell had 92.1% capacity retention after 200 cycles at 0.2C and 79.6% after 1000 cycles at 1C.

The EIS of full cells (Fig. S33, ESI†) followed similar trend as half-cells (Fig. S26, ESI†): Ohmic resistance increased with areal loading, while polarization resistance drastically decreased.

The energy/power densities of co-ESP full cells were summarised in Ragone plots (Fig. 5e and f), compared with previously reported Na-ion full cells.[5,7,69,74,75,77] The co-ESP full cell exhibited maximum gravimetric energy and power densities of 231.6 W h kg^{-1} and 7152.6 W kg^{-1}, respectively. While the maximum areal energy and power densities were 77.7 mW h cm^{-2} and 248.4 mW cm^{-2}, respectively. These performance metrics lead among all reported SIB electrode designs works by significant margin. Thus, uncompromised power and energy were achieved for the co-ESP full cells. Detailed comparisons are provided in Table S9 (ESI†).

Similar with half-cells, the gravimetric energy/power densities of all full cells in Fig. 5e were calculated as in Supplementary Appendix 3 (ESI†). The gravimetric energy/power densities of the co-ESP full cells, considering the electrolyte and separator, are also presented in Fig. S34 (ESI†) to better compare with the industry standard. The results were also compared with Li-ion battery full cells in Table. S11 (ESI†). The energy densities of co-ESP SIB full cells are on par with reported LIBs, while the power densities are notably higher.

To demonstrate the scale-up potential of co-ESP electrodes, we have assembled 0.2 A h pouch cells, which also showed superior performances and stabilities (Fig. 5g). The pouch cells were composed of 100 mg cm^{-2} co-ESP NVPC cathodes and 40 mg cm^{-2} co-ESP HC anodes. The electrolyte's weight was between 1 : 2 to 1 : 2.5 of the electrode active materials.

Cycling stability testing exhibited 75.2% capacity retention after cycling at 0.2C for 1000 cycles (Fig. 5h), which takes nearly a year (361 days). This stability leads among all reported high-areal loading pouch cells.[13] Notably at the 500 cycles the capacity retention is 80.2%, meeting the standard of an iPhone 14 battery (80%, 500 cycles),[85] which demonstrates the practicality and commercialization potential of the high-areal loading co-ESP electrodes. The voltage profiles of the pouch cells are shown in Fig. S35 (ESI†). Considering the mass and volume of the whole cell, co-ESP pouch cell delivered an unprecedented gravimetric energy density of 147 W h kg^{-1}, and a volumetric energy density of 307 W h L^{-1}, one of the highest among all reported SIB pouch cells. The calculation method is detailed in Supplementary Appendix 3 (ESI†). The pouch cell electrodes were compressed under 30 Mpa before pyrolysis. The morphology of the resulting co-ESP NVPC is shown in Fig. S36 (ESI†). From the SEM images, the fibres remain intact under high pressure. There are some microcracks on the NVPC particles, as have been found previously in conventional electrodes after calendaring and were considered to be harmless to the performance of electrodes.[86] Here we also did not observe a notable influence.

Future remarks

We have shown that co-ESP SIB full cells can deliver comparable energy densities and much superior power densities compared to existing LFP-based LIBs while using commercial particles. We have also shown the scaling-up potential of co-ESP method, by producing 600 cm^2 of co-ESP NVPC mat in one batch on a lab-scale electrospinning–electrospraying machine (Fig. 1b). An industry-scale electrospinning/spraying machine has a production capability of over 20 000 000 m^2 per year,[87] equivalent to 12 GW h capacity, assuming a mid-of-range areal loading 60 mg cm^{-2}. It is still difficult to estimate the operating expense of electrospinning due to a lack of public data. But as with other manufacturing technique we expect its cost to be reduced significantly with increasing production scale.[88]

The raw material cost of both the co-ESP and conventional methods is presented in Table S12 (ESI†) for producing 1 kg of NVPC electrodes at a loading of 25 mg cm^{-2} using both the co-ESP and conventional slurry-casting methods (cost obtained from supplier's information online). Since both methods use the same commercially available NVPC particles, we focus on the other raw materials. The co-ESP clearly has a lower cost as the current raw materials' cost stand.

However, raw material prices can fluctuate significantly. This cost analysis is for indicative purposes. The key takeaway is that the co-ESP method offers comparable or lower costs than the conventional methods while providing better energy and power densities.

This suggests the co-ESP SIBs could be rational alternatives for cheaper and quicker electric vehicles in the future. However, the current need for a calcination step in fabricating co-ESP electrodes, which is not part of the standard process for conventional electrodes, presents a major barrier to wider application. Integrating the calcination step into battery manufacturing will be costly and energy-intensive. While there have been effort to directly electrospin conductive fibres,[89] their conductivities are far from enough for battery electrodes. Eliminating the calcination would also drastically reduce the fabrication time of the co-ESP electrode to lower than the conventional electrode, as there is no need for a separate drying process. Therefore, it is necessary to explore novel techniques to electrospin conductive fibres, which will be the focus of our next stage of research.

Materials and methods

Preparation of electrode active materials

The carbon-coated $Na_3V_2(PO_4)_3$ (NVPC) was purchased from Guangdong Canrd New Energy Technology Co., Ltd. The NVPC particles are coated with $\sim$1 wt% carbon on their surface. Hard carbons powder was synthesized by the facile and scalable method reported by literature.[78] The method is that firstly

hydrothermal carbonization of 30 g D-glucose (D-(+)-glucose, ≥99.5%, Sigma-Aldrich) with 270 mL deionized water in an autoclave reactor (50% fill volume) and heated to 230 °C for 12 h; and then the resulting powder was heated at 80 °C under vacuum till fully dried, and finally pyrolysis at 1500 °C (ramping rate 5 °C min^{-1} from room temperature) for 2 h under a continues 500 mL min^{-1} N_2 gas flow.

Electrodes fabrication by co-electrospinning-spraying

The co-ESP electrodes were fabricated through a simultaneous electrospinning–electrospraying method followed by calcination or called co-ESP method. The fabrication set-up is modified from Bioinicia LE-50 electrospinning machine. The schematic of the set-up is shown in Fig. 1a, which consists of two sets of syringes, syringe pumps, and high voltage power supplies for electrospinning and electrospraying respectively. The electrospinning syringe is horizontally placed, and the electrospraying syringe is vertically placed, with a grounded aluminum roller collector placed in the center. Two high voltage power supplies apply adjustable high voltage to two syringes respectively. During fabrication, the rotation speed of the cylindrical collector was set to 50 rpm to avoid any fibre orientation. Both syringes were moving side to side parallel with the collector to ensure uniform thickness.

The fabrication of NVPC/carbon nanotube-carbon nanofibre cathode (NVPC/CNTF) involved simultaneously electrospinning polyacrylonitrile (PAN)/carbon nanotube (CNT) DMF slurry, and electrospraying polyethylene oxide/NVPC DMF slurry. Composition of electrospinning slurry: 5% w/v polyacrylonitrile (PAN, Goodfellow), 1% w/v multi-walled carbon nanotube (MTI) are dissolved/dispersed in dimethylformamide (DMF, Sigma-Aldrich) solvent. To ensure the CNTs are thoroughly dispersed in the electrospinning, we performed a combined method of sonication and stirring of the CNT/DMF dispersant before adding the PAN polymer. More specifically, we performed an 30 min sonication followed by 30 min of vigorous stirring as a cycle, and repeated this cycle for three-times. Composition of electrospraying slurry: 2% w/v PEO (Sigma-Aldrich) and 100% w/v NVPC are dissolved/dispersed in DMF. The total volume and volume ratio of these two slurries were adjusted to fabricate electrodes with different areal loading and active contents. During the fabrication, the distance of electrospinning syringe to roller collector was fixed at 15 cm, distance of electrospraying syringe to the roller 10 cm. The feeding rate of electrospinning slurry is set to 2 mL h^{-1}, feeding rate of electrospraying slurry changes according to the volume ratio of two slurries in order to synchronize the two processes. The voltage applied to the electrospinning syringe was adjusted between 10 to 15 kV to ensure a continuous and drop-free spinning process. Similarly, electrospraying voltage was adjusted between 15 to 20 kV.

The produced NVPC-PEO/CNT-PAN composite mats were peeled off from the roller collector and calcined in 1% H_2/N_2 atmosphere at 850 °C for 5 h, to eliminate PEO and carbonize PAN fibre to carbon fibre (CNF). Finally, co-ESP NVPC cathodes were acquired.

The sub-micron sized NVPC particles were made through ball-milling. 10 g NVPC and 10 mL *tert*-butanol were put in a ball-milling jar. Zirconia balls were used as the milling ball with ball-to-powder ratio of 10 : 1, which were mixed with 1 : 1 : 1 weight ratio of 1-mm, 5-mm and 10-mm zirconia balls. The ball-mill was performed at 100 rpm for 6 hours before freeze drying and collecting the powder. Co-ESP balled-milled NVPC electrodes were made using the ball-milled powder through the same co-ESP process, aiming to acquire the same active content.

To fabricate hard carbon (HC)/CNTF anode, same co-electrospinning-spraying method as above was used. The only difference was that the electrospraying slurry is changed to 2 wt% PEO–50 wt% HC-DMF. The as-prepared HC/PEO/CNF/PAN composite mats were calcined at 1100 °C for 5 h to acquire HC/CNT-CNF anodes.

The co-ESP $LiFePO_4$/C (MTI), SiO_x/C (MTI), and graphite (MTI) electrodes were fabricated using the same co-ESP method as above. The active contents of these electrodes were controlled to be 95 wt%.

Electrodes fabrication by conventional slurry casting

Regarding the hard carbon slurry, 90 wt% hard carbon and 10 wt% pre-prepared sodium carboxymethyl cellulose (CMC, Mw ~ 250 000, Sigma) binder solution (5 wt%) in water were well mixed. Electrodes were coated from slurries onto battery-grade Al foil (17 μm in thickness, MTI) followed by drying at room temperature and ambient environment for 6 hours followed by drying in a vacuum oven for 18 hours. Regarding the NVP slurry, 90 wt% NVP powder, 4 wt% Super P carbon additive (Sigma) and 6 wt% pre-prepared poly(vinylidene fluoride) binder (Mw ~ 534 000, Sigma) solution (5 wt% in N-Methyl-2-pyrrolidone, Sigma) were well mixed. Electrodes were coated from slurries onto battery-grade Al foil (17 μm in thickness, MTI) followed by drying at 80 °C 6 hours followed by drying in a vacuum oven at 80 °C for 18 hours. The mass loading of the resulting electrodes is between ~4 mg cm^{-2} for anode, and ~16 mg cm^{-2} for cathode.

Materials characterization

The morphologies of the electrodes were examined by field emission SEM (Zeiss LEO Gemini 1525 FEGSEM), with an acceleration voltage of 5 kV. The particle and pore size distributions were acquired through image analysis in ImageJ.

The TEM images were acquired by JEOL STEM 2100Plus, with an acceleration voltage of 200 kV.

The phase of the electrodes and raw materials were characterized by X-ray powder diffraction (XRD, X'Pert^3 Powder, Malvern Panalytical). The Raman spectrum was performed on a Renishaw inVia confocal Raman microscope, using 532 nm laser.

Thermogravimetric analysis (TGA) was performed on a Netzsch STA449C. TGA experiments were performed in air and nitrogen atmosphere, under 5 °C min^{-1} ramping rating.

The microscope assisted nano-scale X-ray tomography (nano-CT) was performed in diamond synchrotron I-13-2 beamline. The energy was of X-ray was 8 eV and 1950 images were acquired by continuously rotating the sample 180 degrees using an integration time of 1.8 s per radiograph. The spatial resolution was 47 nm and field of view was 150 × 150 × 150 μm.

Image reconstruction was carried out using a bespoke routine implemented by the I-13-2 beamline scientists.

Micron-scale X-ray tomography (micron-CT) was performed at the European synchrotron radiation facility (ESRF) beamline ID19. The energy of X-ray was 16 keV and 1800 images were acquired by continuously rotating the sample 180 degrees using an integration time of 1 s per radiograph. The linear resolution was 350 nm, with a large field of view of 1 × 1 × 1 mm. Image reconstruction was carried out using a bespoke routine implemented by the ID19 beamline scientists.

The reconstructed images from CTs were analysed in the Avizo software, from which the microstructural parameters including volume contents, porosity, pore tortuosity and porosity distribution were extracted.[90,91]

The in-plane conductivity was measured on an Ossila four-point conductivity tester. The through-plane conductivities were measured by a potentiostat (Metrohm Autolab PGSTAT302N).

The strain–stress curve of co-ESP NVPC electrodes were acquired from the compressive mechanical testing, which was performed on a ZwickRoell ZwickiLine universal testing machine. The sample sizes were 2 × 2 cm^2.

Electrochemical characterisation

The electrochemical properties of the electrodes were examined in CR2032 coin cells, assembled in an argon-filled glove box with water and oxygen content both lower than 1 ppm. For high-areal loading co-ESP NVP electrodes, no spacer or spring is needed when assembling the cells. All cells were tested on a biologic ultra-precision battery cycler at 25 °C. When assembling half-cells, electrodes (co-ESP electrodes and conventional electrodes) were used directly as cathodes. Sodium metal was rolled and punched into 12 mm-diameter round chips and used as anodes. Celgard 2400 polypropylene membranes were used as separators. 1 M $NaPF_6$ (Canrd) in ethylene carbonate (EC)/diethyl carbonate (DEC) (EC/DEC = 1 : 1, v/v%, Sigma-Aldrich) with 10% fluoroethylene carbonate (FEC) (Sigma-Aldrich) was used as the electrolyte. The amount of electrolyte is controlled to 3 : 1 mass ratio relative to the electrode.

The NVPC half-cells were cycled in a voltage range of 2.0–3.8 V. The HC half-cells were cycled in a voltage range of 0.005–2.5 V.

The full cells were assembled using NVPC electrodes (co-ESP electrodes and conventional electrodes) as the cathodes, and HC electrodes (co-ESP electrodes and conventional electrodes) as the anodes. Celgard 2400 polypropylene membranes were used as separators. 1 M $NaPF_6$ in ethylene carbonate (EC)/dimethyl carbonate (DEC) (EC/DEC = 1 : 1, v/v%) was used as the electrolyte. The full cells were cycled in a voltage range of 0.5–3.8 V. In the cycling of NVPC half-cells and full cells, the charging processes were done in a constant current–constant voltage (CC–CV) mode. In the CC stage, cells were charged to 3.8 V under constant current. Then in the CV stage, the cells were charged with 3.8 V voltage until the current reach 0.05C.

The impedance measurements of all cells were performed on the biologic ultra-precision battery cycler with a frequency range of 0.1 to 10 kHz, an amplitude of 10 mV was used. All measurements were conducted in a fully discharged state.

The Na-ion monolayer pouch cell was constructed using 40 mg cm^{-2} co-ESP hard carbon as the anodes and 100 mg cm^{-2} co-ESP NVPC as the cathodes. Both electrodes were pressed under 30 MPa to flatten the electrodes, ensuring their good contact with the separator. The electrolyte consisted of 1 M $NaPF_6$ in a solvent mixture of EC and DEC, mixed in a 1 : 1 volume ratio. A Celgard 2400 separator was positioned between the anode and cathode and soaked in the electrolyte solution to ensure sufficient ionic transport during cell operation. The thickness of aluminum plastic film is 90 μm, weight 14 mg cm^{-2}.

The assembly of the pouch cell was performed layer-by-layer in an ambient environment because both hard carbon and NVP are resistant to humidity. The separator was sandwiched between the anode and cathode, and three ends of the layered assembly were sealed first, before being placed in an antechamber of a glovebox for drying at 80 °C for 18 hours. After drying, the pouch cell was transferred to the glovebox where oxygen and moisture levels were maintained below 5 ppm, and allowed to cool to room temperature. Then, an electrolyte of 1 M $NaPF_6$ in EC/DEC was injected into the pouch cell, followed by vacuum sealing the final end. The edges of the pouch were heat-sealed at 180 °C for 4 seconds to securely encapsulate the electrodes and electrolyte. The sealed cell rested at room temperature for 12 hours before any electrochemical testing to ensure good wettability of both electrodes and the separator.

For pre-sodiation, the pouch cell was constructed with a piece of Na metal positioned against the co-ESP hard carbon electrode, separated by a piece of Celgard 2400. A three-electrodes set-up as described in a previous work was applied to monitor the voltages of cathode and anode individually.[78] The assembly was completed inside a glovebox (O_2 and H_2O levels less than 0.5 ppm). The assembled pouch cell rested for 18 hours before undergoing formation cycles (constant current mode at 30 mA g^{-1}, voltage window from 10 mV to 2.0 V). After pre-sodiation, the pouch cell was opened inside a glovebox to prevent exposure to oxygen and humidity. The pre-sodiated co-ESP hard carbon electrode was then transferred from one pouch cell to another. It is important to note that during this transfer, a negligible amount of carbon content was lost due to mechanical forces, which could not be measured.

Then the electrolyte is filled to the pouch cell with a similar process as referenced:[92] we initially filled the pouch cells with excess electrolyte (1 : 1 ratio of electrolyte to active material, or 10 g A h^{-1}) followed by vacuum sealing. Then we clamped the cells, allowed them to rest for 12 hours, and cycled at 30 mA g^{-1} for one cycle to ensure proper wetting and formation. Afterward, the pouch cell is opened in the glovebox and the excess electrolyte was extracted, followed by a second vacuum-sealing and degassing process. The final electrolyte amount in pouch cell is 1 : 2 to 2.5 of the weight of active material amount.

The three-electrode pouch cells were tested on biologic channels, while or the three-electrode pouch cells were tested on Land CT3002A channels.

Conclusions

In this study, we developed an electrode fabrication technique by concurrently electrospinning CNTF conductive backbones and electrospraying carbon-coated $Na_3V_2(PO_4)_3$ (co-ESP NVPC) onto identical substrates.

Our in-depth 2D and 3D morphology characterizations revealed that the NVPC particles are bound to the CNTF network by spatial constriction, ensuring all pores remain fully accessible for unhindered Na-ion transport. The electrospun CNTF network, while constituting merely 2.5 wt% of the content, adeptly serves as a binder, conductive additive, and current collector, ensuring electronic connectivity to all NVPC particles.

Due to the fast species transportation and robust structure, the co-ESP NVPC electrodes exhibited superior rate-performance and stability. Notably, particles larger than the pore of CNTF network proved to have better performance than their smaller counterparts as the electrosprayed species. The sturdy CNTF networks facilitated the production of extremely high-areal-loading electrodes with up to 296 mg cm^{-2} areal loading.

Both coin cells and pouch cells, with co-ESP electrodes showed state-of-art and uncompromised energy and power densities, even comparable to lithium-ion batteries, demonstrating the merit of co-ESP method.

Finally, the co-ESP is a promising fabrication method to greatly enhance the energy/power density of battery electrode. It is applicable to a variety of commercial cathode and anode materials of Na-ion batteries and Li-ion batteries and is scalable, demonstrating its commercialization potential.

Author contributions

M. Ouyang conceived the project, designed the experiments, developed the novel fabrication methods and supervised the project. M. Ouyang, G. Li, F. Li fabricated the novel electrodes. M. Ouyang, Z. Guo and K. Zheng assembled the coin cells and conducted electrochemical tests. Z. Guo and K. Zheng assembled the pouch cells and conducted electrochemical tests. M. Ouyang, L. E. S. Farran and S. Zhao performed the CT characterization. L. E. S. Farran performed image processing and analysis. M. Ouyang, H. Zhang, Z. Guo, M. Wang and F. Li performed the physical characterizations. Y. Zhao contributed to the experimental design and the development of electrode fabrication. X. Liu, S. Yang, M. Titirici and N. Brandon contributed to the experimental design and the manuscript modification. M. Ouyang and Z. Guo wrote the original manuscript. All authors analysed the data and proof-read the manuscript.

Data availability

The data that support the findings of this study are available from the corresponding author, MO, upon reasonable request.

Conflicts of interest

There are no conflicts to declare.

Acknowledgements

M. O. would like to thank the funding support from EPSRC (EP/W032589/1). Z. G. and M. T. would like to thank the grants from Faraday institute (NEXGENNA, reference number: FIRG064). S. Z. acknowledges funding from the Faraday Institution (EP/S003053/1) under the degradation project (FIRG060). The authors would like to acknowledge diamond light source for time on beamline I13-2 under proposal MG-34782, especially we would like to thank Dr Leonard Turpin for his assistance in finishing the session. The authors would like to acknowledge the European Synchrotron Radiation Facility (ESRF) for provision of synchrotron radiation facilities under proposal MA-5933 and we would like to thank Dr Benoit Cordonnier for assistance and support in using beamline ID19.

Notes and references

1 J.-M. Tarascon, *Joule*, 2020, **4**, 1616–1620.
2 P. K. Nayak, L. Yang, W. Brehm and P. Adelhelm, *Angew. Chem., Int. Ed.*, 2018, **57**, 102–120.
3 X. Xiang, K. Zhang and J. Chen, *Adv. Mater.*, 2015, **27**, 5343–5364.
4 J. Yang, D. Li, X. Wang, X. Zhang, J. Xu and J. Chen, *Energy Storage Mater.*, 2020, **24**, 694–699.
5 Q. Wei, X. Chang, J. Wang, T. Huang, X. Huang, J. Yu, H. Zheng, J.-H. Chen and D.-L. Peng, *Adv. Mater.*, 2022, **34**, 2108304.
6 L. Gao, S. Chen, L. Zhang and X. Yang, *ChemElectroChem*, 2019, **6**, 947–952.
7 Z. Lv, M. Yue, M. Ling, H. Zhang, J. Yan, Q. Zheng and X. Li, *Adv. Energy Mater.*, 2021, **11**, 2003725.
8 L. Hu, F. La Mantia, H. Wu, X. Xie, J. McDonough, M. Pasta and Y. Cui, *Adv. Energy Mater.*, 2011, **1**, 1012–1017.
9 S.-H. Park, P. J. King, R. Tian, C. S. Boland, J. Coelho, C. Zhang, P. McBean, N. McEvoy, M. P. Kremer, D. Daly, J. N. Coleman and V. Nicolosi, *Nat. Energy*, 2019, **4**, 560–567.
10 Y. Kuang, C. Chen, D. Kirsch and L. Hu, *Adv. Energy Mater.*, 2019, **9**, 1901457.
11 T. Zhang and F. Ran, *Adv. Funct. Mater.*, 2021, **31**, 2010041.
12 Y. Zhang, F. Li, K. Yang, X. Liu, Y. Chen, Z. Lao, K. Mai and Z. Zhang, *Adv. Funct. Mater.*, 2021, **31**, 2100434.
13 M. Ryu, Y.-K. Hong, S.-Y. Lee and J. H. Park, *Nat. Commun.*, 2023, **14**, 1316.
14 F. Hippauf, B. Schumm, S. Doerfler, H. Althues, S. Fujiki, T. Shiratsuchi, T. Tsujimura, Y. Aihara and S. Kaskel, *Energy Storage Mater.*, 2019, **21**, 390–398.
15 X. Lu, A. Bertei, D. P. Finegan, C. Tan, S. R. Daemi, J. S. Weaving, K. B. O'Regan, T. M. M. Heenan, G. Hinds, E. Kendrick, D. J. L. Brett and P. R. Shearing, *Nat. Commun.*, 2020, **11**, 2079.

16 H. Sun, L. Mei, J. Liang, Z. Zhao, C. Lee, H. Fei, M. Ding, J. Lau, M. Li and C. Wang, *Science*, 2017, **356**, 599–604.
17 L.-L. Lu, Y.-Y. Lu, Z.-J. Xiao, T.-W. Zhang, F. Zhou, T. Ma, Y. Ni, H.-B. Yao, S.-H. Yu and Y. Cui, *Adv. Mater.*, 2018, **30**, 1706745.
18 J. T. Lee, C. Jo and M. De Volder, *Proc. Natl. Acad. Sci. U. S. A.*, 2020, **117**, 21155–21161.
19 H. Li, L. Peng, D. Wu, J. Wu, Y.-J. Zhu and X. Hu, *Adv. Energy Mater.*, 2019, **9**, 1802930.
20 H. Wang, J. Fu, C. Wang, R. Zhang, Y. Yang, Y. Li, C. Li, Q. Sun, H. Li and T. Zhai, *Adv. Funct. Mater.*, 2021, **31**, 2102284.
21 R. Tian, S.-H. Park, P. J. King, G. Cunningham, J. Coelho, V. Nicolosi and J. N. Coleman, *Nat. Commun.*, 2019, **10**, 1933.
22 Y. Orikasa, Y. Gogyo, H. Yamashige, M. Katayama, K. Chen, T. Mori, K. Yamamoto, T. Masese, Y. Inada, T. Ohta, Z. Siroma, S. Kato, H. Kinoshita, H. Arai, Z. Ogumi and Y. Uchimoto, *Sci. Rep.*, 2016, **6**, 26382.
23 X. Li, W. Chen, Q. Qian, H. Huang, Y. Chen, Z. Wang, Q. Chen, J. Yang, J. Li and Y.-W. Mai, *Adv. Energy Mater.*, 2021, **11**, 2000845.
24 S. Cavaliere, S. Subianto, I. Savych, D. J. Jones and J. Rozière, *Energy Environ. Sci.*, 2011, **4**, 4761–4785.
25 O. H. Kwon, J. H. Oh, B. Gu, M. S. Jo, S. H. Oh, Y. C. Kang, J.-K. Kim, S. M. Jeong and J. S. Cho, *Adv. Sci.*, 2020, **7**, 2001358.
26 A. M. Boyce, X. Lu, D. J. L. Brett and P. R. Shearing, *J. Power Sources*, 2022, **542**, 231779.
27 Z. Li, J. T. Zhang, Y. M. Chen, J. Li and X. W. Lou, *Nat. Commun.*, 2015, **6**, 8850.
28 M. Zhang, M. Chouchane, S. A. Shojaee, B. Winiarski, Z. Liu, L. Li, R. Pelapur, A. Shodiev, W. Yao, J.-M. Doux, S. Wang, Y. Li, C. Liu, H. Lemmens, A. A. Franco and Y. S. Meng, *Joule*, 2023, **7**, 201–220.
29 M. Kroll, S. L. Karstens, M. Cronau, A. Höltzel, S. Schlabach, N. Nobel, C. Redenbach, B. Roling and U. Tallarek, *Batteries Supercaps*, 2021, **4**, 1363–1373.
30 J. Wang, H. Xu, Y. Huo, Y. Wang and M. Dong, *Nanotechnology*, 2020, **31**, 132001.
31 Y. Xu, Y. Zhu, F. Han, C. Luo and C. Wang, *Adv. Energy Mater.*, 2015, **5**, 1400753.
32 J.-M. Kim, C.-H. Park, Q. Wu and S.-Y. Lee, *Adv. Energy Mater.*, 2016, **6**, 1501594.
33 C. Zhu, Y. Fu and Y. Yu, *Adv. Mater.*, 2019, **31**, 1803408.
34 S. Wang, S. Li, Y. Sun, X. Feng and C. Chen, *Energy Environ. Sci.*, 2011, **4**, 2854–2857.
35 E. Zussman, X. Chen, W. Ding, L. Calabri, D. A. Dikin, J. P. Quintana and R. S. Ruoff, *Carbon*, 2005, **43**, 2175–2185.
36 R. Fang, K. Chen, L. Yin, Z. Sun, F. Li and H.-M. Cheng, *Adv. Mater.*, 2019, **31**, 1800863.
37 T. Morimoto, K. Kobashi and T. Okazaki, *J. Phys. Chem. C*, 2021, **125**, 19362–19367.
38 D. Simien, J. A. Fagan, W. Luo, J. F. Douglas, K. Migler and J. Obrzut, *ACS Nano*, 2008, **2**, 1879–1884.
39 D. Almecija, D. Blond, J. E. Sader, J. N. Coleman and J. J. Boland, *Carbon*, 2009, **47**, 2253–2258.
40 T. Maitra, S. Sharma, A. Srivastava, Y.-K. Cho, M. Madou and A. Sharma, *Carbon*, 2012, **50**, 1753–1761.
41 J. K. W. Sandler, J. E. Kirk, I. A. Kinloch, M. S. P. Shaffer and A. H. Windle, *Polymer*, 2003, **44**, 5893–5899.
42 J. Shim and J. H. Bang, *J. Energy Chem.*, 2023, **82**, 56–65.
43 R. Chowdhury, Y. Zhao, Y. Xia, M. Ouyang, N. Brandon and A. Banerjee, *Sustainable Energy Fuels*, 2021, **5**, 5193–5204.
44 Z. Zhang, J. Yang, W. Huang, H. Wang, W. Zhou, Y. Li, Y. Li, J. Xu, W. Huang, W. Chiu and Y. Cui, *Matter*, 2021, **4**, 302–312.
45 C. Zhu, R. E. Usiskin, Y. Yu and J. Maier, *Science*, 2017, **358**, eaao2808.
46 J. Zheng, R. Garcia-Mendez and L. A. Archer, *ACS Nano*, 2021, **15**, 19014–19025.
47 L. Almar, J. Joos, A. Weber and E. Ivers-Tiffée, *J. Power Sources*, 2019, **427**, 1–14.
48 K. Yang, L. Yang, Z. Wang, B. Guo, Z. Song, Y. Fu, Y. Ji, M. Liu, W. Zhao, X. Liu, S. Yang and F. Pan, *Adv. Energy Mater.*, 2021, **11**, 2100601.
49 R. Jervis, M. D. R. Kok, J. Montagut, J. T. Gostick, D. J. L. Brett and P. R. Shearing, *Energy Technol.*, 2018, **6**, 2488–2500.
50 $Na_3V_2(PO_4)_3$ ($Na_3V_2[PO_4]_3$ ht$_3$) Crystal Structure: Datasheet from "PAULING FILE Multinaries Edition – 2022", in SpringerMaterials. Springer-Verlag Berlin Heidelberg & Material Phases Data System (MPDS), Switzerland & National Institute for Materials Science (NIMS), Japan, **https://materials.springer.com/isp/crystallographic/docs/sd_1520006**.
51 E. J. Cheng, K. Hong, N. J. Taylor, H. Choe, J. Wolfenstine and J. Sakamoto, *J. Eur. Ceram. Soc.*, 2017, **37**, 3213–3217.
52 $LiFePO_4$ (LiFe[PO_4] rt) Crystal Structure: Datasheet from "PAULING FILE Multinaries Edition – 2022", in SpringerMaterials, Springer-Verlag Berlin Heidelberg & Material Phases Data System (MPDS), Switzerland & National Institute for Materials Science (NIMS), Japan, **https://materials.springer.com/isp/crystallographic/docs/sd_1031132**.
53 T. Hutzenlaub, A. Asthana, J. Becker, D. R. Wheeler, R. Zengerle and S. Thiele, *Electrochem. Commun.*, 2013, **27**, 77–80.
54 A. Mistry, S. Trask, A. Dunlop, G. Jeka, B. Polzin, P. P. Mukherjee and V. Srinivasan, *J. Electrochem. Soc.*, 2021, **168**, 070536.
55 B. Ludwig, Z. Zheng, W. Shou, Y. Wang and H. Pan, *Sci. Rep.*, 2016, **6**, 23150.
56 S. Chen, J. Lin, Q. Shi, Z. Cai, L. Cao, L. Zhu and Z. Yuan, *J. Electrochem. Soc.*, 2020, **167**, 080506.
57 M. D. Obradović, G. D. Vuković, S. I. Stevanović, V. V. Panić, P. S. Uskoković, A. Kowal and S. L. Gojković, *J. Electroanal. Chem.*, 2009, **634**, 22–30.
58 Z. Y. Jiang, Z. G. Qu, L. Zhou and W. Q. Tao, *Appl. Energy*, 2017, **194**, 530–539.
59 A. Chauhan, E. Asylbekov, S. Kespe and H. Nirschl, *Electrochem. Sci. Adv.*, 2023, **3**, e2100151.
60 S. Chen, C. Wu, L. Shen, C. Zhu, Y. Huang, K. Xi, J. Maier and Y. Yu, *Adv. Mater.*, 2017, **29**, 1700431.
61 A. Ponrouch, R. Dedryvère, D. Monti, A. E. Demet, J. M. Ateba Mba, L. Croguennec, C. Masquelier, P. Johansson and M. R. Palacín, *Energy Environ. Sci.*, 2013, **6**, 2361–2369.

62 J. Entwistle, R. Ge, K. Pardikar, R. Smith and D. Cumming, *Renewable Sustainable Energy Rev.*, 2022, **166**, 112624.
63 L. Qie, C. Zu and A. Manthiram, *Adv. Energy Mater.*, 2016, **6**, 1502459.
64 R. Rodriguez, K. E. Loeffler, S. S. Nathan, J. K. Sheavly, A. Dolocan, A. Heller and C. B. Mullins, *ACS Energy Lett.*, 2017, **2**, 2051–2057.
65 J. Lee, Y. Lee, J. Lee, S.-M. Lee, J.-H. Choi, H. Kim, M.-S. Kwon, K. Kang, K. T. Lee and N.-S. Choi, *ACS Appl. Mater. Interfaces*, 2017, **9**, 3723–3732.
66 M. E. Sotomayor, C. D. L. Torre-Gamarra, B. Levenfeld, J.-Y. Sanchez, A. Varez, G.-T. Kim, A. Varzi and S. Passerini, *J. Power Sources*, 2019, **437**, 226923.
67 W. Duan, M. Husain, Y. Li, N. U. R. Lashari, Y. Yang, C. Ma, Y. Zhao and X. Li, *RSC Adv.*, 2023, **13**, 25327–25333.
68 B. Shi, Y. Shang, Y. Pei, S. Pei, L. Wang, D. Heider, Y. Y. Zhao, C. Zheng, B. Yang, S. Yarlagadda, T.-W. Chou and K. K. Fu, *Nano Lett.*, 2020, **20**, 5504–5512.
69 Y. Geng, T. Zhang, T. Xu, W. Mao, D. Li, K. Dai, J. Zhang and G. Ai, *Energy Storage Mater.*, 2022, **49**, 67–76.
70 C.-Y. Yu, J.-S. Park, H.-G. Jung, K.-Y. Chung, D. Aurbach, Y.-K. Sun and S.-T. Myung, *Energy Environ. Sci.*, 2015, **8**, 2019–2026.
71 W. Ren, Z. Zheng, C. Xu, C. Niu, Q. Wei, Q. An, K. Zhao, M. Yan, M. Qin and L. Mai, *Nano Energy*, 2016, **25**, 145–153.
72 Q. Fan, Y. Zhang, Q. Xu, J. Wang, L. Lei, Y. Sun and P. D. Lund, *Energy Storage Mater.*, 2019, **21**, 457–463.
73 N. Ogihara, Y. Itou, T. Sasaki and Y. Takeuchi, *J. Phys. Chem. C*, 2015, **119**, 4612–4619.
74 J. Hwang, K. Matsumoto and R. Hagiwara, *ACS Appl. Energy Mater.*, 2019, **2**, 2818–2827.
75 H. Song and K. Eom, *Adv. Funct. Mater.*, 2020, **30**, 2003086.
76 Z. Lv, M. Ling, H. Yi, H. Zhang, Q. Zheng and X. Li, *ACS Appl. Mater. Interfaces*, 2020, **12**, 13869–13877.
77 S. Yu, Z. Liu, H. Tempel, H. Kungl and R.-A. Eichel, *J. Mater. Chem. A*, 2018, **6**, 18304–18317.
78 Z. Guo, Z. Xu, F. Xie, J. Jiang, K. Zheng, S. Alabidun, M. Crespo-Ribadeneyra, Y.-S. Hu, H. Au and M.-M. Titirici, *Adv. Mater.*, 2023, 2304091n/a.
79 J. Zhu, C. Chen, Y. Lu, Y. Ge, H. Jiang, K. Fu and X. Zhang, *Carbon*, 2015, **94**, 189–195.
80 P. Bai, X. Han, Y. He, P. Xiong, Y. Zhao, J. Sun and Y. Xu, *Energy Storage Mater.*, 2020, **25**, 324–333.
81 A. P. Vijaya Kumar Saroja, M. Muruganathan, K. Muthusamy, H. Mizuta and R. Sundara, *Nano Lett.*, 2018, **18**, 5688–5696.
82 Y. Wan, Y. Liu, D. Chao, W. Li and D. Zhao, *Nano Mater. Sci.*, 2023, **5**, 189–201.
83 M. Dahbi, T. Nakano, N. Yabuuchi, S. Fujimura, K. Chihara, K. Kubota, J.-Y. Son, Y.-T. Cui, H. Oji and S. Komaba, *ChemElectroChem*, 2016, **3**, 1856–1867.
84 M. Singh, J. Kaiser and H. Hahn, *J. Electrochem. Soc.*, 2015, **162**, A1196.
85 A. Inc., *iPhone battery and performance*, **https://support.apple.com/en-gb/101575**.
86 T. Günther, D. Schreiner, A. Metkar, C. Meyer, A. Kwade and G. Reinhart, *Energy Technol.*, 2020, **8**, 1900026.
87 S. Omer, L. Forgách, R. Zelkó and I. Sebe, *Pharmaceutics*, 2021, **13**, 286.
88 E. Atzeni and A. Salmi, *Int. J. Adv. Des. Manuf. Technol.*, 2012, **62**, 1147–1155.
89 X.-X. Wang, G.-F. Yu, J. Zhang, M. Yu, S. Ramakrishna and Y.-Z. Long, *Prog. Mater. Sci.*, 2021, **115**, 100704.
90 L. Salinas-Farran, A. Batchelor and S. J. Neethling, *Hydrometallurgy*, 2022, **207**, 105776.
91 L. Salinas-Farran, W. Brownscombe, F. Iacoviello, P. R. Shearing, P. Brito-Parada and S. J. Neethling, *Miner. Eng.*, 2024, **213**, 108762.
92 F. J. Günter, C. Burgstaller, F. Konwitschny and G. Reinhart, *J. Electrochem. Soc.*, 2019, **166**, A1709.